Memoirs of the Faculty of Engineering, Nagoya University
Vol. 40, No. 1 (1988) -Research Report-

# ROLE OF TRANSVERSE WAVES IN A DETONATION WAVE - A STUDY BASED ON PROPAGATION IN A POROUS WALL CHAMBER

K.V. REDDY, TOSHI FUJIWARA and J.H. LEE

*Department of Aeronautical Engineering*

(Received May 31, 1988)

**Abstract**

A mathematical model is constructed to study the role of transverse waves in a detonation wave. The lower solid wall in a two-dimensional channel is replaced with a porous wall that absorbs momentum and energy but does not allow mass to leave the system. A plane Chapman-Jouguet (C-J) ZND detonation wave is disturbed by putting a few exothermic spots in the neighborhood of the leading shock-front to generate a stable multi-dimensional detonation wave. All the elementary reactions occurring behind a leading shock are represented by a two-step reaction model. The mathematical model is developed by treating the entire flow as a two-stream fluid flow: Main flow in the channel is solved using the MacCormack second-order explicit finite-difference scheme while the capillary flow in the porous wall using an upwind finite-difference scheme. Both solutions are then coupled through the boundary conditions. By changing the porosity of the porous wall, propagation of the detonation wave is controlled. Numerical calculations are made for different channel widths and different porosities. Various interesting phenomena such as detonation quenching, development of galloping detonations and penetration of a shock wave into an expansion zone are demonstrated.

## 1. Introduction

The Zel'dovich-von Neumann-Döring (ZND) model[1] is the most successful concept in understanding the Chapman-Jouguet (C-J) detonation. However, this one-dimensional detonation wave model as a shock discontinuity followed by a zone of chemical reaction after a certain ignition delay has been shown dynamically unstable.[2] In fact, a number of careful experimental observations confirmed that all detonations propagated with a

complex nonsteady frontal structure of shocks. This shock system consists of a number of triple shocks traveling also in the transverse direction to the main flow. Recently, based on a two-dimensional stability analysis, Buckmaster[3] predicted the development of very large pressure spots in a plane detonation wave starting from small-amplitude perturbations. He argued that such high pressure spots ultimately developed into Mach stems and hence transverse waves. All these studies are directed toward the establishment of stable multi-dimensional detonation wave.

Taki and Fujiwara[4,5] were successful in simulating these shocks numerically in two dimensions. By destructing a one-dimensional ZND detonation wave with some added exothermicity spots they obtained a stable nonsteady detonation. They also re-established that though the instantaneous propagation velocity widely varied from the C-J value, the wave traveled at an average velocity close to the C-J value.

Once established, the transverse waves are essential to have a stable detonation; then questions arise about the strength and role of these transverse waves in a detonation wave. It is very interesting to know how these unstable detonation waves respond to any action that suppresses transverse waves. Quenching of detonation or adjusting to an under-driven detonation wave are not the only outcome of this duel between establishing and suppressing actions on transverse waves. When a climax is reached, the unburnt gas pockets[6] formed in the burnt gas explode to generate a galloping detonation which re-establishes a multi-dimensional detonation wave from a dying detonation wave.

Therefore, naturally, a number of studies are initiated to understand the role of transverse waves on the propagation of a detonation wave. Recent experiments by Dupre[7] indicate that the damping of transverse waves by acoustically attenuating walls caused a detonation to fail. The small air pockets in a porous wall act like a hydraulic damper to absorb momentum, effective only when there is a pressure jump. Thus, when a shock wave hits a porous wall, the detonation loses a portion of its momentum and gets reflected as a relatively weak shock. This hydraulic damping on the shock can be utilized in suppressing the transverse waves in a detonation wave and thereby one can have better understanding on the role of transverse waves. The present paper describes a numerical model to simulate a multi-dimensional detonation wave that is traveling in a chamber with a porous wall.

## 2. Mathematical Formulation

Although a porous material has cellular structure with numerous interconnected free air cells (see upper wall in Fig. 1), all the dynamic behaviors related to this material can be simulated by modeling it as a rigid wall with a large number of thin and long circular cylindrical capillary tubes (lower wall in Fig. 1). All these tubes are open on one side that is in contact with the flow, while the other sides are sealed so that no mass is allowed to leave the system. Schematic sequential changes of the flow due to the porous wall are also depicted in Fig. 1. For a low damping coefficient of the porous wall, a detonation wave propagates stably in an

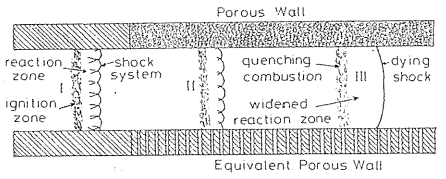


Fig. 1. Real and modeled equivalent porous walls and schematic description of the problem.

under-driven detonation mode. A wide induction zone may be observed in such flows. When the damping coefficient is above a critical value, significant momentum in the transverse waves is absorbed into the porous wall and the detonation soon fails because of the weak transverse waves.

The entire flow can be regarded as a two-stream fluid flow with the main flow and the capillary flow in porous tubes.

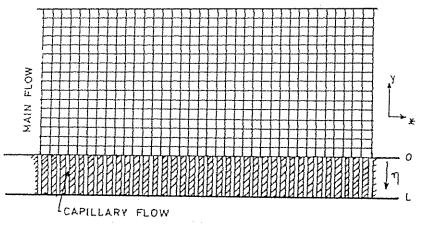


Fig. 2. The grid system used for the main and capillary flows.

*Main Flow*:

A simplified model is used to describe a detonation wave. All the elementary reactions occurring behind a leading shock wave are represented by a two-step reaction model of induction and exothermic reactions[5] containing two reaction progress variables $\alpha$ and $\beta$. The specific reaction rate of the induction reaction is given by

$$W_\alpha \equiv \frac{d\alpha}{dt^*} = -\frac{1}{\tau_{ind}} = -K_1 \rho^* exp(-E_1/RT^*), \tag{1}$$

and that for the exothermic reaction is given by

$$W_\beta \equiv \frac{d\beta}{dt^*} \begin{cases} = 0, & \alpha > 0, \\ = -K_2 p^{*2}[\beta^2 exp(\frac{E_2}{RT^*}) - (1-\beta)^2 exp(-\frac{E_2+Q^*}{RT^*})], & \alpha \leqq 0. \end{cases} \tag{2}$$

Here the superscript * indicates the dimensional values and the reaction parameters appearing in Eqs. (1) and (2) are selected as

$$K_1 = 3.0 \times 10^{11} cm^3/g/s, \quad K_2 = 1.5 \times 10^{-7} cm^4/dyn^2/s,$$

$$E_1/R = 9800K, \quad E_2/R = 2000K \ and \ Q^* = 4.0 \times 10^{10} erg/g,$$

to fit either $2H_2+O_2+7Ar$ or $2H_2+O_2+7He$ mixture.
The fundamental governing equations under perfect gas, inviscid and non-heat-conducting assumptions can be written in the following non-dimensional conservation-law form:

$$\frac{\partial q}{\partial t} + \frac{\partial E}{\partial x} + \frac{\partial F}{\partial y} + H = 0, \tag{3}$$

where the inviscid flux vectors and the chemical source term vector are

$$q = \begin{pmatrix} \rho \\ \rho u \\ \rho v \\ e \\ \rho\beta \\ \rho\alpha \end{pmatrix}, \quad E = \begin{pmatrix} \rho u \\ \rho u^2 + p \\ \rho uv \\ (e+p)u \\ \rho u\beta \\ \rho u\alpha \end{pmatrix}, \quad F = \begin{pmatrix} \rho v \\ \rho uv \\ \rho v^2 + p \\ (e+p)v \\ \rho v\beta \\ \rho v\alpha \end{pmatrix} \ and \ H = \begin{pmatrix} 0 \\ 0 \\ 0 \\ 0 \\ -\rho W_\beta \\ -\rho W_\alpha \end{pmatrix}.$$

The state equations

$$p=(\gamma-1)[e-\rho\beta Q-0.5\rho(u^2+v^2)], \tag{4}$$

$$p=\beta_0\rho T, \tag{5}$$

are also used to complete the system of Eq. (3). The following non-dimensionalization is used in the above formulation:

$$t=\frac{t^*}{\ell^*}a_\infty{}^*, \quad x,y=\frac{x^*,y^*}{\ell^*}, \quad u,v=\frac{u^*,v^*}{a_\infty{}^*}, \quad \rho=\frac{\rho^*}{\rho_\infty{}^*},$$
$$e=\frac{e^*}{\rho_\infty{}^* a_\infty{}^{*2}}, \quad Q=\frac{Q^*}{a_\infty{}^{*2}} \quad and \quad T=\frac{T^*}{T_\infty{}^*}, \tag{6}$$

and the constant in Eq. (5) appearing due to non-dimensionalization is defined as

$$\beta_0=\frac{R}{a_\infty{}^{*2}}T_\infty{}^*.$$

*Capillary Flow*:

The porous material is assumed to consist of an aggregation of long thin tubes, within which a polytropic motion of the gas is governed by the balance between the pressure gradient and viscous force alone; the irregular character of most porous materials is therefore ignored in this simple model. By assuming that inertial effects of the gas motion within a long tube of very small diameter and the variations of pressure across any tube cross section can be neglected,[8] the fluid motion within the porous medium is mathematically formulated as follows:

Defining $\eta$ as the coordinate along the tube axis (see Fig. 2), the approximate momentum equation is

$$p_\eta-\frac{\beta_1}{r}(r\ v_r')_r=0, \tag{7}$$

with

$$\beta_1=\mu^*/\rho_\infty{}^* a_\infty{}^* L^*,$$

where $v'$ is the non-dimensional axial ($\eta$-direction) velocity, $r$ is the non-dimensional radial coordinate, L* the tube length and $\mu^*$ the dynamic viscosity. Assuming that $\mu^*$ is constant and $v'$ is zero when $r=a$ ($a^*$ is the tube radius) and using the hypothesis that $p_\eta$ is a function of $\eta$ and $t$ only, integration of Eq. (7) with respect to $r$ yields

$$v'=\left(-\frac{p_\eta}{4\beta_1}\right)(a^2-r^2) \tag{8}$$

The mean velocity $\hat{v}$ across any plane perpendicular to $\eta$ is given by

$$\hat{v}=\frac{2}{a^2}\int_0^a rv'\,dr, \tag{9}$$

$$=-D_c p_\eta, \tag{10}$$

where $D_c=a/8\beta_1$. This relation between the mean velocity and the mean pressure gradient is a particular form of the Darcy's resistance law; the parameter is constant for a given porous material.

The continuity equation of gas within the tube can be written as

$$\rho_t+(\rho\hat{v})_\eta=0. \tag{11}$$

One may propose that the fluid flow inside a thin tube obeys a polytropic law, i.e.

$$p=K\rho^m, \tag{12}$$

where $K$ and $m$ are the constants with $1<m<\gamma$ where $\gamma$ is equal to the usual specific heats ratio. For such flows, Eq. (11) can be rewritten as

$$p_t+mp^{1-\frac{1}{m}}(p^{\frac{1}{m}}\hat{v})_\eta=0. \tag{13}$$

Eqs. (10) and (13) form an initial-value problem for the variables $p$ and $\hat{v}$.

## 3. Boundary Conditions

Eqs. (3) to (5) for the main flow and Eqs. (10) and (13) for the capillary flow are coupled only through the boundary conditions; hence, they can be solved independently, once the flow variables $p$ and $\hat{v}$ are known at the matching boundary i.e. at y=$\eta$=0. The boundary conditions for Eqs. (10) and (13) are

$$\hat{v}=0 \qquad at\ \eta=L, \tag{14}$$

$$p=p_e(x,t) \quad at\ \eta=0. \tag{15}$$

Here $p_e(x,t)$ is the external flow as far as porous flow is concerned and is solely determined by the main flow. Boundaries for the main flow are the solid upper wall and the porous lower wall. At the solid wall reflection principle is used to impose flow tangency conditions. At the porous wall the normal velocity component $\hat{v}$ is set equal to the value that is obtained from the capillary flow solution at $\eta=0$ and all the other variables except $p$ are extrapolated from the field points. Pressure $p_e(x,t)$ is then determined by solving Eq. (4). Usually at any time $t$ an iteration is required to obtain the matching pressure $p_e(x,t)$ and $\hat{v}$ at $\eta$=y=0, and is described in the following section.

## 4. Numerical Scheme

The main and capillary flows are to be solved numerically to acquire a consistent solution. Eqs. (3) to (5) are solved using the second-order MacCormack finite-difference scheme. The predictor and corrector steps of the scheme are as follows:

*Predictor:*

$$q^{(1)}_{i,j}=q^{n}_{i,j}-\frac{\Delta t}{\Delta x}(E^{n}_{i+1,j}-E^{n}_{i,j})-\frac{\Delta t}{\Delta y}(F^{n}_{i,j+1}-F^{n}_{i,j})-\Delta t\ H^{n}_{i,j}\ . \tag{16}$$

*Corrector:*

$$\hat{q}^{n+1}_{i,j}=\frac{1}{2}[q^{n}_{i,j}+q^{(1)}_{i,j}-\frac{\Delta t}{\Delta x}(E^{(1)}_{i,j}-E^{(1)}_{i-1,j})-\frac{\Delta t}{\Delta y}(F^{(1)}_{i,j}-F^{(1)}_{i,j-1})-\Delta t\ H^{(1)}_{i,j}]\ . \tag{17}$$

In order to reduce the spurious oscillations near shocks and to make the shocks steeper the fourth-order diffusion terms and flux corrected transport (FCT) limiters are added. They are given by

*Fourth-order Diffusion:*

$$\begin{aligned}\bar{q}^{n+1}_{i,j}=\hat{q}^{n+1}_{i,j}&-\mu_x(q^{n}_{i-2,j}-4q^{n}_{i-1,j}+6q^{n}_{i,j}-4q^{n}_{i+1,j}+q^{n}_{i+2,j})\\&-\mu_y(q^{n}_{i,j-2}-4q^{n}_{i,j-1}+6q^{n}_{i,j}-4q^{n}_{i,j+1}+q^{n}_{i,j+2}).\end{aligned} \tag{18}$$

*FCT Limiters:*

$$\bar{q}^{n+1}_{i,j}=\bar{q}^{n+1}_{i,j}+\eta_x(q^{n}_{i+1,j}-2q^{n}_{i,j}+q^{n}_{i-1,j}),\ \ \bar{\bar{q}}^{n+1}_{i,j}=\bar{q}^{n+1}_{i,j}+\eta_y(q^{n}_{i,j+1}-2q^{n}_{i,j}+q^{n}_{i,j-1}), \tag{19}$$

$$q^{n+1}_{i,j}=\bar{q}^{n+1}_{i,j}+\bar{\bar{q}}^{n+1}_{i,j}-\bar{q}^{n+1}_{i,j}-(\delta^{c}_{i+\frac{1}{2},j}-\delta^{c}_{i-\frac{1}{2},j})-(\delta^{c}_{i,j+\frac{1}{2}}-\delta^{c}_{i,j-\frac{1}{2}}), \tag{20}$$

where

$$\begin{aligned}&\delta^{c}_{i+\frac{1}{2},j}=S\cdot Max[0,\ Min(S\cdot\Delta_{i-\frac{1}{2},j},\ |\tilde{\Delta}_{i+\frac{1}{2},j}|,\ S\cdot\Delta_{i+\frac{3}{2},j})],\\&\Delta_{i+\frac{1}{2},j}=\bar{q}^{n+1}_{i+1,j}-\bar{q}^{n+1}_{i,j},\\&\tilde{\Delta}_{i+\frac{1}{2},j}=\eta_x(\tilde{q}^{n+1}_{i+1,j}-\tilde{q}^{n+1}_{i,j}),\\&S=Sign(\tilde{\Delta}_{i+\frac{1}{2},j})\ .\end{aligned}$$

The governing Eqs. (10) and (13) for the capillary flow are solved by using an upwind finite-difference scheme,

$$p^{n+1}_{k}=p^{n}_{k}-\frac{\Delta t}{\Delta\eta}\{(p^{n}_{k})^{1-\frac{1}{m}}\ [(p^{n}_{k+1})^{\frac{1}{m}}\ \hat{v}^{n}_{k+1}-(p^{n}_{k})^{\frac{1}{m}}\ \hat{v}^{n}_{k}]\}, \tag{21}$$

and

$$\hat{v}_k^{n+1} = - \frac{D_c}{\Delta \eta}[p_{k+1}^{n+1} - p_k^{n+1}]. \tag{22}$$

As mentioned earlier, the solution procedure involves an iteration procedure, since the pressure and velocity at the matching boundary are coupled through the main and capillary flows. Based on the velocities in the capillary tubes at n-th time step, Eqs. (16) through (20) are solved first for the pressure at (n+1)-th time step. At this pressure, Eqs. (21) and (22) are solved for the flow in a capillary tube. Using this new velocity, calculations are repeated to correct the main flow and then the capillary flow at (n+1)-th time step; this cycle has to be continued until convergence. Usually two iterations are sufficient.

## 5. Results and Discussions

All the calculations are started from a plane C-J ZND detonation wave. A stable multi-dimensional detonation wave is generated by placing exothermic spots just upstream of the leading shock front. These exothermic spots perturb the plane C-J wave and develop transverse waves. Once the detonation becomes stable then the lower wall is replaced by a porous wall. By changing the wall porosity, studies on the role of transverse waves on detonation propagation are made. The grids are constructed with $\Delta x = 2/9$ and $\Delta y = \Delta \eta = 2/9$. Though L, the depth of the porous wall, is a parameter to determine the Darcy's coefficiennt, it is held constant at 20 and the value of Darcy's coefficient is varied by changing the other parameters such as $a^*$ and $\mu^*$.

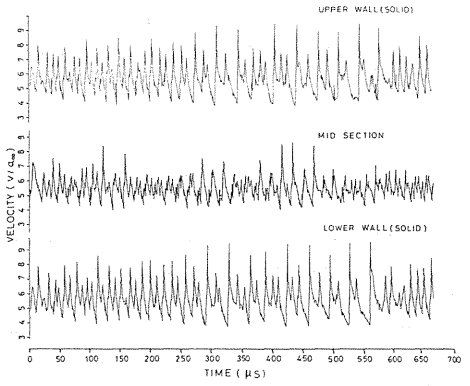


Fig. 3. The propagation velocity of a detonation front along three locations, the upper and lower walls and the center line, for a 9 $\ell^*$-wide channel with both solid walls.

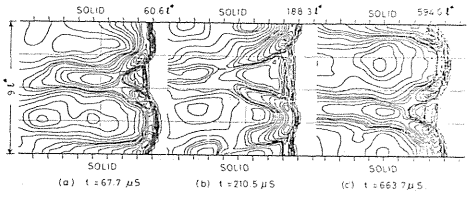


Fig. 4. History of detonation wave structure in terms of pressure contours in a 9 $\ell^*$-wide channel with both solid walls. Average non-dimensional propagation velocity is found to be 4.96.

*Channel with both solid walls:*

To make sure that the present analysis is able to generate a stable multi-dimensional detonation wave, both of the walls of a 9 $\ell^*$-wide channel are made solid boundaries and calculations are carried out for 7000 time steps. By this time the detonation front has moved by 66 channel widths corresponding to the 663.7 $\mu$s real time. The wave velocities at the lower and upper walls and at the mid section are plotted in Fig. 3, while the wave-front structure at three different times is depicted in Fig. 4. The detonation wave is found to be very stable with three transverse waves. The average non-dimensional propagation velocity is 4.96, which is close to the C-J velocity for the mixture considered ($D_{C-J}$=4.8). These calculations are made on a 44 × 500 grid system for which a FUJITSU-VP200 computer took 4.96 × $10^{-6}$ s/step/grid cpu time.

*4 $\ell^*$ channel with a porous wall:*

Lower wall of a 4 $\ell^*$-wide channel is replaced by a porous wall of Darcy's coefficient equal to 0.02. The plane C-J detonation wave is disturbed by the porous channel itself. The shock-front velocities at the walls and at the mid section are plotted in Fig. 5, while

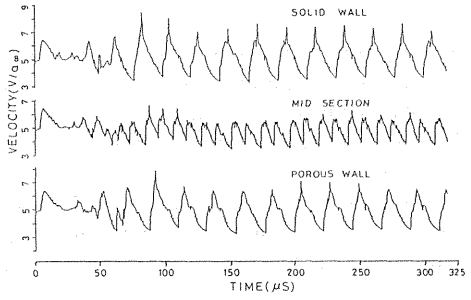


Fig. 5. Propagation velocity of a detonation wave as a function of time at the upper solid and lower porous walls and along the center line, in a 4 $\ell^*$-wide channel having the Darcy's coefficient $D_c$=0.02.

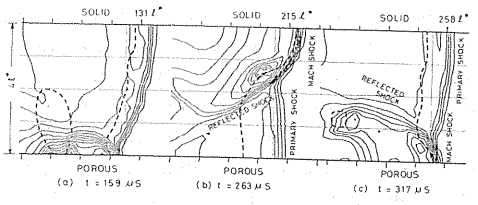


Fig. 6. History of detonation wave structure in terms of pressure contours in a 4 $\ell^*$-wide channel with solid upper and porous lower (Darcy's coefficient $D_c$=0.02) walls. The average detonation propagation velocity is reduced from 4.96 to 4.46.

the shocks at three different times are shown in Fig. 6. At this porosity, a stable detonation wave with one transverse wave is established. The velocity fluctuations at the mid section appear at a frequency twice that at the walls because a single transverse shock leaving from a wall crosses the center line two times before it again reaches the same wall. Average propagation velocity of the detonation is found to be 4,46, which is less than the C-J value 4.80 and is 89.92 percent of that in a solid wall chamber (note that the propagation velocity 4.96 obtained in a 9 $\ell^*$-wide channel remains almost at the same value in a 4 $\ell^*$-wide channel). This indicates that the weakened transverse shock ultimately reduces the detonation propagation velocity. Broken lines in the shock structure plots show the reaction front, giving the induction length. A marked feature on detonation wave structure due to the porous wall may be seen in the induction length. As seen in

Fig. 6, this 4 $\ell^*$-wide channel supports only one triple shock and, after following the notation used by Strehlow,[9] the wave structure can be identified as the combined Mach shock, primary shock and reflected shock. The Mach shock which supports the detonation propagation associates with a shorter induction zone and fast exothermic reaction. Under the presence of the porous wall, the strength of the Mach shock is not essentially affected and as a result stable propagation is made possible. On the other hand, the weakened transverse shock balances the flow with the help of a weak primary shock wave. This can also be identified in the wave structure showing the increased induction zones associated with the primary shock waves. In Figs. 6(b) and 6(c) it may also be noted that the induction lengths associated with the incident shocks standing on the porous wall and solid wall are different. The transverse wave, when it impinges the porous wall, loses a portion of its momentum and gets reflected as a weak transverse wave and hence the induction distance associated with the primary shock standing on the porous wall is longer. This difference in the primary shocks leads to an irregular wave front in a multi-cell detonation. As the difference in the induction zone lengths of the Mach shock and primary shock increases in a detonation wave, each collision of triple point with the wall generates a pocket of unburnt gas. Presence of unburnt gas has been observed in experiments by Subbotin[10] and in numerical simulations by Oran.[6] These pockets are completely surrounded by burnt gas and most of them in turn burn more slowly, finally giving their energy to the system. Explosive burning of the unreacted trapped gas depends on the particular condition in and outside the pocket.

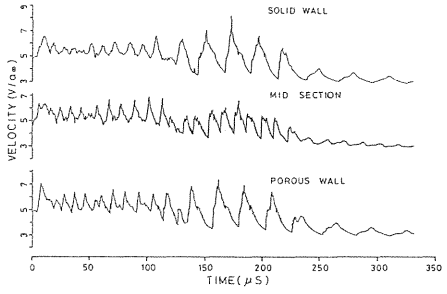


Fig. 7. Propagation velocity of a detonation wave as a function of time at the upper solid and lower porous walls and along the center line, in a 4 $\ell^*$-wide channel having the Darcy's coefficient $D_c$=0.035. At t=230 microsec the detonation gets decoupled and the propagation velocity rapidly decreases.

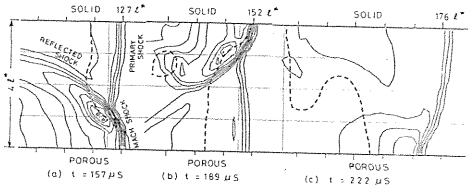


Fig. 8. History of detonation wave structure in terms of pressure contours in a 4 $\ell^*$-wide channel with solid upper and porous lower (Darcy's coefficient $D_c$=0.035) walls.

By increasing the porosity of the lower wall ($D_c$=0.035), calculations are repeated. Similar plots are shown in Figs. 7 and 8. At this porosity, the detonation wave is unable to self-sustain and dies after traveling for 230 $\mu$s. The highly porous wall continuously absorbs momentum from the transverse wave. Once the strength of the transverse wave is reduced below a critical value, it can no longer support the detonation wave and as a result the detonation is quenched soon.

Typical velocity distribution at the open ends of capillary tubes at a particular instant of time is shown in Fig. 9. When the detonation wave front passes over a capillary tube, the gas is pushed into the tube to balance the pressure jump. The steep increase in the velocity in Fig. 9 represents arrival of the wave front. The small negative velocity before the shock wave is due to the undershoot in the calculated pressure. The viscous fluid in the capillary tube gradually transmits the external pressure toward the sealed end and this settles the fluid in the tube. The other two velocity jumps seen in the figure are due to the slapping of transverse waves on the porous wall in the burnt gas region.

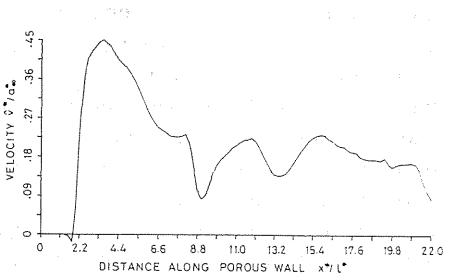


Fig. 9. Non-dimensional velocity distribution at the open ends of the capillary tubes along the porous wall at a particular instant of time.

*9 $\ell^*$ channel with a porous wall:*

Calculations are made for a detonation within a 9 $\ell^*$-wide channel with a porous lower wall and a solid upper wall. Results for two Darcy's coefficients ($D_c$=0.06 and 0.08)

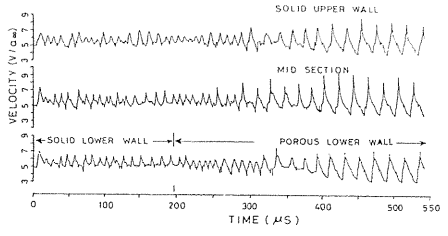


Fig. 10. Propagation velocity of a detonation wave as a function of time at the upper solid and lower porous walls and along the center line, in a 9 $\ell^*$-wide channel having the Darcy's coefficient $D_c$=0.06. The number of triple shocks settles down to 2 after t=300 microsec.

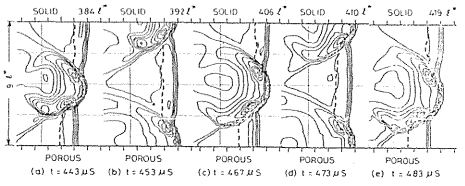


Fig. 11. History of detonation wave structure in terms of pressure contours in a 9 $\ell^*$-wide channel with solid upper and porous lower (Darcy's coefficient $D_c$=0.06) walls. A stable detonation with two transverse waves is developed.

are shown in Figs. 10 through 13. For these calculations the lower wall is made porous only after 197 $\mu$s; by that time a stable detonation is developed within a solid wall chamber. For $D_c$=0.06 a stable detonation with two transverse waves is developed. For the same channel width but with both solid walls a channel was able to generate a stable detonation wave with three transverse waves (See Fig. 4). This indicates that the transverse waves in a channel with a porous wall are not uniformly weakened but are one by one weakened before being completely absorbed in a queue. As the number of

absorbed transverse waves increases, the remaining transverse waves are either strong enough or not enough to keep the detonation alive in the whole width of the channel. This confirms that the number of transverse waves depends on the width of the channel. In Fig. 11 it can be observed that a weak and a strong transverse shocks are forming an irregular wave front. The difference in the induction lengths associated with the primary shocks standing on porous and solid walls can also be identified in Figs. 11(a), (c), and (e). These transverse waves are in fact moving toward the walls and the primary shock on a wall was generated by the transverse wave that is penetrating into the other primary shock. This irregular wave front is stable in a chamber with a wall replaced by a porous wall and the stability can be argued as follows: In Fig. 11(a), the strong transverse shock is moving toward the porous wall and the weak transverse shock toward the solid wall. After 10 microseconds these strong and weak shocks get reflected from the porous and solid walls, respectively as weak and strong transverse waves (Fig. 11(b)). These two reflected shocks moving toward the center of the channel are crossed (Fig. 11(c)) at a section slightly shifted toward the porous wall from the mid section. The shock front at 467 $\mu$s is identical to the shock fronts at 443 $\mu$s and also at 483 $\mu$s, indicating a stable propagation of the irregular wave front. The detonation is propagating at a velocity equal

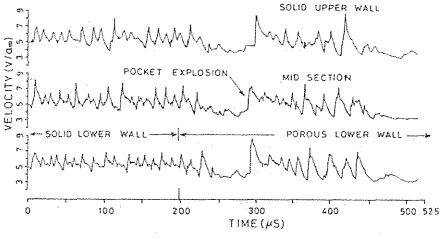


Fig. 12. Propagation velocity of a detonation wave as a function of time at the upper solid and lower porous walls and along the center line, in a 9 $\ell^*$-wide channel having the Darcy's coefficient $D_c$=0.08. At t=230 microsec the detonation gets decoupled, followed by coupling at t=300 microsec, and again decoupled at t=420 microsec; a galloping is observed due to the explosion of an unburnt pocket in burnt environment.

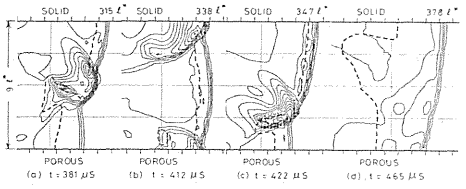


Fig. 13. How a detonation gets decoupled in galloping mode is seen in the history of detonation wave structure in terms of pressure contours in a 9 $\ell^*$-wide channel with solid upper and porous lower (Darcy's coefficient $D_c$=0.08) walls. The detonation front is losing another tripple shock at t=422 microsec.

to 4.84, which is 2.42 percent less than the corresponding velocity in a solid wall chamber. For $D_c$=0.08, the detonation fails after 450 microseconds. Before failure, the wave front is very irregular as seen in Fig. 13(a). In Fig. 13(c) it is noticed that the shock front is losing yet another transverse wave. The remaining transverse wave is not sufficient to maintain the detonation. In fact, at time 250 $\mu$s, the detonation fails once (see Fig. 12). But due to pocket explosion of a trapped unburnt gas, the detonation is re-established.

*Galloping Detonations:*

From the velocity profiles on the walls and mid section in Fig. 12, it can be observed that at time 250 $\mu$s the detonation loses all its transverse waves and is dying. At 295 $\mu$s the detonation is re-established back to a galloping mode. As discussed earlier, certain particular conditions cause the unburnt gas that is trapped within burnt gas to explode. It may not be of any interest to a combustion researcher if the shock wave generated from the explosive burning ultimately dies out within the reacted gas. But when the explosion of unburnt gas occurs close to the heated unburnt gas within the induction zone of a detonation wave front, the shock from pocket explosion eventually develops into a galloping detonation. The sequence occurring between the time 260 $\mu$s and 292 $\mu$s is shown in Figs. 14(a) through (1). The wave structure within a solid wall chamber at t=188 $\mu$s is shown in Fig. 14(a). When this wave enters into a porous wall chamber, it loses all its transverse shocks as shown in Fig. 14(b) at t=260 $\mu$s. A weak triple shock may be identified but this does not do anything helpful and the detonation finally dies out. At time 271 $\mu$s, an unburnt gas pocket is isolated at the solid wall (Fig. 14(c)). Along with the unreacted gas pocket, an unburnt peninsula in the induction zone is also found at t=271 $\mu$s. The explosive burning of this trapped unreacted gas generates shock waves that are traveling in all directions. Since the tongue of the peninsula is sufficietnly close to the burning trapped gas pocket, the shock waves are able to reach the peninsula (Fig. 14(d)). These weak shock waves are sufficient to initiate burning of the already heated gas in the peninsula (Fig. 14(e)). At time t=283 $\mu$s (Fig. 14(f)), the whole gas in the peninsula has been burnt, resulting into a strong explosion. In Fig. 14(g) this explosion gathers more and more energy by penetrating into the induction zone and eventually forms a galloping detonation wave. The propagation velocity of this galloping wave is much higher than that of the dying wave. Due to the structure of the formed induction zone, this galloping detonation wave gets a velocity component toward the porous wall (Fig. 14(h)). At time t=283 $\mu$s, the galloping detonation hits the porous wall (Fig. 14 (i)) before it catches up with the dying front wave. A careful observation of the pressure plots gives some idea about the structure of the galloping detonation wave. The blast wave has a structure with a shock wave in the outer shell and expansion waves in the inner core. The expansion waves headed by a shock wave are moving toward the porous wall and front wave. Therefore, when this galloping detonation hits the porous wall, then the reflection process contains two effects: One is, due to the porosity of the wall surface, the reflection of the incident shock as a weaker shock. Due to the trailing expansion waves, this reflected shock penetrates into the expansion zone which weakens the shock. These two effects can be seen in Figs. 14(i) to (l) and as a result the reflected shock becomes very weak. Meanwhile, at t=287 $\mu$s (Fig. 14(j)), the galloping detonation catches up with the dying shock wave and re-establishes the detonation wave having two triple shocks. The other stem of the galloping detonation wave still having strong expansion waves at its back is moving toward the solid wall and hits it at t=294 $\mu$s (Fig. 15(a)). The shock wave immediately gets reflected and is penetrating into the expansion zone as seen in Fig. 15(b). The reflection process ends with a resulting transverse shock and the re-established detonation wave now is supported by the two transverse shocks indicated as $t_1$ and $t_2$ in Fig. 15(c) at t=296.5 $\mu$s. After a few reflections of these transverse shocks from walls, the detonation wave develops into an irregular wave front shown in Fig. 13(a) at t=381 $\mu$s. Without any further appearance of periodical galloping, the wave dies after t=450 $\mu$s. A channel which supports more transverse waves is more susceptible to the galloping detonation and hence detonation failure in a very wide channel due to porous wall is most unlikely.

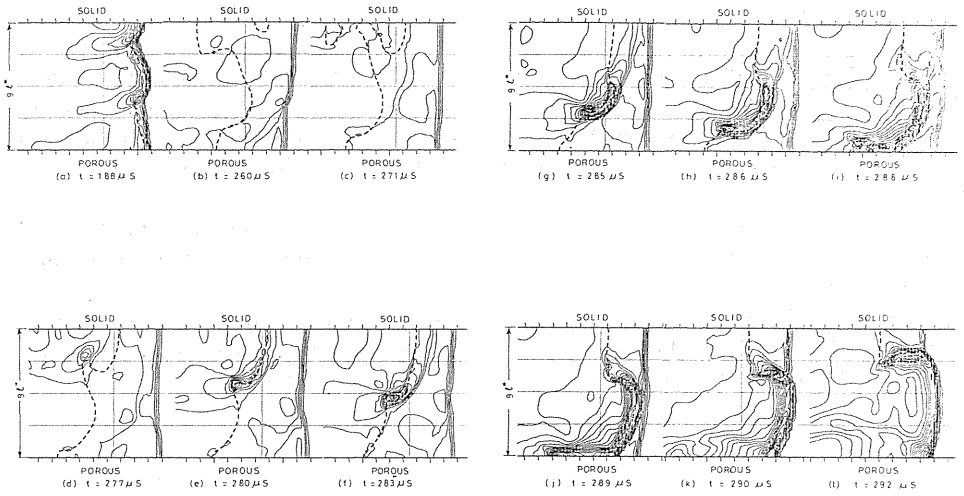


Fig. 14. Cinematographic view of a galloping detonation (case of Fig. 13):
(a) A detonation wave with three triple shocks propagating in a solid-solid channel is exposed to a solid-porous channel.
(b) A dying detonation wave.
(c) Generation of an unreacted gas pocket.
(d) Gas pressure builds up due to the explosion of the isolated gas pocket.
(e) Due to the blast wave, a concave peninsula-shape reaction front is accelerated to the forward direction.
(f) Explosion of unreacted gas in the peninsula and buildup of a very strong shock wave.
(g) Amplification of the local explosion due to the generation of the shock wave.
(h) The development of a reacting shock wave.
(i) Interaction of the shock with the lower porous wall and simultaneous interaction between the reacting shock and leading inert shock.
(k) Formation of a triple shock and disappearance of the shock reflected from the porous wall.
(l) Completion of a double-headed detonation wave.

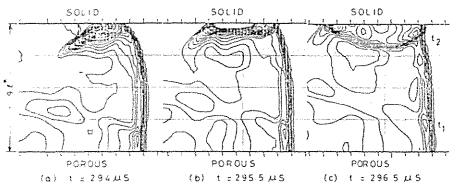


Fig. 15. The instant of reflection from the solid wall for a transverse wave in the galloping detonation.

## 6. Conclusions

A mathematical model to generate a detonation in a channel with a porous wall is developed. This model is quite useful for studying the role of transverse waves on detonation propagation. The following observations are made during the present study:

1. A stable detonation that travels at a speed lower than the C-J value can be established in a chamber with porous walls.

2. Porous walls do not attenuate all the transverse waves simultaneously; instead they weaken and absorb one by one in a queue. In other words porous walls increase the cell size and reduce the number of cells.

3. Due to the irregularity of the wave front, pockets of unburnt gas are formed frequently, and their explosion can occur, giving a mechanism of detonation galloping. As a result, a detonation in a porous chamber is fairly unpredictable.

## References

1) Williams, F.A., Combustion Theory, Addison-Wesley Publishing Company, Mass., 1985. pp. 182–228.
2) Abouseif, G. and Toong, T.Y.; Theory of Unstable One-Dimensional Detonations, Combustion and Flame. 45, 1982, pp. 67.
3) Buckmaster, J.D.; Series of lectures given on Stability of Detonation Waves' at the Department of Aeronautical Engineering, Nagoya University between May 30, 1988 and June 2, 1988.
4) Taki, S. and Fujiwara, T., Numerical Analysis of Two-Dimensional nonsteady Detonations. AIAA J. Vol. 16, No. 1, Jan. 1978.
5) Taki, S. and Fujiwara T.; Numerical Simulation of Triple Shock Behavior of Gaseous Detonation, Eighteenth Symposium (International) on Combustion, p. 1671. The Commustion Institute, 1981.
6) Oran, E.S., Young, T.R., Boris, J.P., Picone, J.M., and Edwards, D.H.; A study of Detonation Structure: The Formation of Unreacted Gas Pockets, Nineteenth Symposium (International) on Combustion, p. 573, The Combustion Institute, 1982.
7) Dupre, G., Propagation of Detonation Waves in an Acoustic absorbing-Walled Tube, 11 the International Colloquium on Dynamics of Explosions and Reactive Systems, Warszawa, Aug. 1987.
8) Clarke, J.F., The Reflection of Weak Shock Waves from Absorbent Surfaces, Proc. Roy. Soc. London, A396, pp. 365–382, 1984.
9) Roger A. Strehlow, Gas Phase Detonations: Recent Developments, Combustion & Flame, 12, No. 2, 1968, pp. 81–101.
10) Subbotin, V.A.; Fizika Goreniya i vzryva 11, 96 (1975).